

Implications of Grid-Forming Inverter Parameters on Disturbance Localization and Controllability

Matt Baughman, Marena Trujillo, Bri-Mathias Hodge, Emily Jensen*

Department of Electrical, Computer & Energy Engineering
University of Colorado Boulder

Boulder, Colorado, United States

{matt.baughman, marena.trujillo, ejensen, brimathias.hodge}@colorado.edu

Abstract—The shift from traditional synchronous generator (SG) based power generation to generation driven by power electronic devices introduces new dynamic phenomena and considerations for the control of large-scale power systems. In this paper, two aspects of all-inverter power systems are investigated: greater localization of system disturbance response and greater system controllability. The prevalence of both of these aspects are shown to be related to the lower effective inertia of inverters and have implications for future wide-area control system design. Greater disturbance localization implies the need for feedback measurement placement close to generator nodes to properly reject disturbances in the system while increased system controllability implies that wide-area control systems should preferentially actuate inverters to most efficiently control the system. This investigation utilizes reduced-order linear time-invariant models of both SGs and inverters that are shown to capture the frequency dynamics of interest in both all-SG and all-inverter systems, allowing for the efficient use of both frequency and time domain analysis methods.

I. INTRODUCTION

The share of power-electronic generation has grown rapidly in the 21st century as solar PV, wind, and battery storage, all of which require an inverter, have become cost-competitive with conventional generation [1]. Inverter-based resources (IBRs) are generally classified as Grid-Following (GFL) or Grid-Forming (GFM) [2]. GFLs regulate AC current and rely on a phase-locked loop (PLL) to track the grid frequency [3], meaning another device must “form” the grid. Synchronous generators (SGs) naturally provide this function by establishing their own voltage and frequency [4]. Today, GFLs operate in mixed SG-IBR systems where SGs supply the grid-forming capability [3]. GFMs, in contrast, establish voltage and frequency through closed-loop control and are therefore essential for all-IBR power systems [2]. Among various GFM implementations, this paper focuses on multi-loop droop-controlled GFMs that use $P-\omega$ droop to maintain synchronization [5].

While the dynamics of systems of SGs have been widely analyzed [4], legacy methods may not be applicable to IBR-dominated power systems characterized by fast dynamics and low inertia values [6]. The fast dynamics from IBRs and the increasing deployment of new measurement systems in large-scale power systems available for feedback control

has made the implementation of wide-area control systems (WACs) both necessary and feasible [7]. To inform wide-area control design decisions, an interpretable connection between IBR design parameters and IBR-dominated system behavior and controllability is necessary.

System controllability refers to how much energy is needed to control the system along a state trajectory and can be quantified by the eigenvalues of the controllability gramian [8]. Many studies have evaluated the controllability of systems of SGs [9]–[11], and more recently, there have been efforts to assess the controllability of systems with some amount of IBRs. For instance, in [12], the controllability of a 100% IBR microgrid is assessed to determine how controller flexibility may be utilized to support small-signal stability. In [13], the modal controllability matrix of a power system with wind turbines is used for the optimal aggregation of an impedance network model. Analytical expressions for performance metrics related to frequency stability are presented in [14] under the assumption of proportional machine parameters. This paper complements these recent works by providing a connection between GFM parameters and system disturbance response and controllability, allowing for an interpretable connection between GFM design decisions and system behavior. This paper presents a novel assessment of the impact of effective GFM inertia on disturbance localization and system controllability. Increased disturbance localization under high GFM penetration scenarios is demonstrated, motivating the need for strategic feedback measurement locations in a wide-area control policy. Additionally, evidence of the increased controllability of GFM-dominated systems is presented, indicating the importance of actuating GFMs for the efficient control of future system dynamics.

II. REDUCED ORDER MODEL

The main result of this paper will be analytical relationships between GFM parameters and system behavior. To achieve this, we leverage the reduced-order linear time invariant models of SG and GFM frequency dynamics proposed in [15]. This section offers a physical interpretation of GFM model parameters that will motivate the rest of the analysis.

A. Model Summary

The network representation is based on the Kron-reduced DC power flow equation, where only generator nodes are

* Corresponding author. This work was supported by National Science Foundation (NSF) under Grant ECCS-2527653.

retained [15].

$$\Delta P_G = \mathbf{B}_r \Delta \delta_G + \mathbf{B}_L \Delta P_L \quad (1)$$

where G denotes generator buses and L denotes non-generator buses. The Δ prefix indicates a deviation from nominal. Note that \mathbf{B}_r is the reduced network Laplacian and matrix \mathbf{B}_L maps a change in power at a non-generator bus to the change in power injection by a generator bus.

The SG model used is shown in block diagram form in Figure 1. M and D refer to the inertia and damping coefficients of the generator's shaft, respectively. The governor is connected in feedback with an input of frequency. K represents the governor and turbine response gain, R_{SG} is the droop coefficient, T_{SG} is the governor and turbine response time constant, and ω_0 is the nominal generator frequency. The parameter α is the ratio of the system base power to the device rated capacity [15].

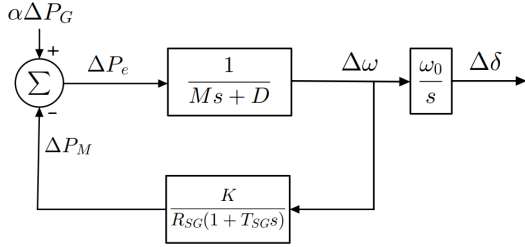


Fig. 1: Block diagram for the SG model [15].

The model of a multi-loop droop GFM is shown in block diagram form in Figure 2. R represents the GFM droop coefficient and T_c represents the time constant of the GFM's power measurement filter [15].

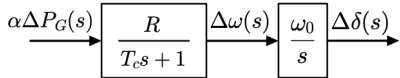


Fig. 2: Block diagram for grid forming inverter model [15].

B. Interpreting the GFM Inverter Model

The GFM model utilized is a first-order transfer function with the following relationship between change in GFM power and change in GFM frequency:

$$\frac{\Delta \omega(s)}{\alpha \Delta P_G(s)} = \frac{1}{\frac{T_c}{R} s + \frac{1}{R}} \quad (2)$$

In the SG model, the transfer function representing the shaft dynamics maps a change in electrical power to a change in frequency, while in the GFM the outer-loop droop controller is responsible for this mapping. In both the SG and GFM models, this transfer function is first order, and this parallel can be used to understand GFM dynamics in a more traditional framework. In this framework, the effective inertia of the droop GFM is equal to $M_{eff} = \frac{T_c}{R}$ and the effective damping defined as $D_{eff} = \frac{1}{R}$. Under the assumption that all GFMs have identical effective inertia, damping and rated

capacity, a system of n GFM nodes and m load nodes can be written as a system of ODEs with the following state vector:

$$x = [\Delta \delta_1 - \Delta \delta_n \dots \Delta \delta_{n-1} - \Delta \delta_n \ \Delta \dot{\delta}_1 \dots \Delta \dot{\delta}_n]^T \quad (3)$$

$$\dot{x} = \begin{bmatrix} 0_{n-1 \times n} & 1_{-1} \\ \frac{\tilde{\mathbf{B}}_r}{M_{eff}} & \frac{-D_{eff}}{M_{eff}} I_n \end{bmatrix} x + \begin{bmatrix} 0_{n-1 \times m} \\ \frac{\alpha}{M_{eff}} \mathbf{B}_L \end{bmatrix} \begin{bmatrix} \Delta P_{L_1} \\ \vdots \\ \Delta P_{L_m} \end{bmatrix} \quad (4)$$

I_n refers to the $n \times n$ identity matrix, 1_{-1} is a matrix defined as $1_{-1} = [I_{n-1} \ -1_{n-1 \times 1}]$, $\tilde{\mathbf{B}}_r$ refers to \mathbf{B}_r with the n -th column removed.

We assume a power measurement time constant of $T_C = 0.0318$ s and a droop coefficient of $R = 0.05$ (or 5% droop), which yields an effective inertia of $M_{eff} = 0.636$ and effective damping of $D_{eff} = 20$. Compared to standard SG inertia and damping values which range from 2 to 9 and 1 to 2, respectively [4], the GFM effective inertia is roughly an order of magnitude smaller than usual SG inertia values while the effective damping is roughly an order of magnitude greater; however, parameters can be tuned to modify the GFM's response due to the digital nature of GFM controls [16]. An analytical interpretation of how these GFM parameters impact system behavior is discussed in the next section.

III. ANALYSIS OF DISTURBANCE LOCALIZATION IN ALL-GFM SYSTEMS

To create an interpretable relationship between system behavior and GFM parameters, a simple three-GFM system model provides an illustrative example. This model assumes that line admittance coupling all generators to each other is identical and all GFMs share the same effective inertia and damping. The simple model emulates a Kron-reduced system, where each generator is connected to the others in a triangle network topology. For readability, the effective inertia of the GFM (the ratio of time constant to droop coefficient) is written as M and the effective damping (the inverse of the droop coefficient) is written as D based on the physical interpretation of these parameters discussed in Section II. Here, we derive and compare the transfer functions of a generator's response to a disturbance occurring 1) at the generator's bus, and 2) at a different generator's bus. The symmetry of the system means that only these two transfer functions are needed to describe the system. Then, the transfer functions are used to derive the poles and zeros of the system for both the local and nonlocal disturbance response of the GFMs in the system. The location of the poles and zeros can then be used to understand how GFM parameters relate to the localization of disturbances. The derived transfer functions will also be used to form analytical expressions for the H_2 -norm of the GFM's local and nonlocal response, a common metric used to measure responsiveness in power systems [17], to further show how effective GFM inertia impacts responses to local and nonlocal disturbances.

A. Pole-Zero Analysis

The derived expressions relating the changes in net generator power at each generator node to changes in generator frequency form a 3×3 symmetric, circulant transfer function matrix where diagonal and off-diagonal terms are defined as:

$$\begin{aligned}\Delta\omega_i(s) &= \frac{\frac{M}{B}s^2 + \frac{D}{B}s + 1}{(\frac{M}{B}s^2 + \frac{D}{B}s + 3)(Ms + D)} \Delta P_{L_i}(s) \\ \Delta\omega_i(s) &= \frac{1}{(\frac{M}{B}s^2 + \frac{D}{B}s + 3)(Ms + D)} \Delta P_{L_j}(s), i \neq j\end{aligned}\quad (5)$$

Both diagonal and off-diagonal transfer functions have three poles:

$$p = \frac{-\frac{D}{B} \pm \sqrt{\frac{D^2}{B^2} - 12\frac{M}{B}}}{2\frac{M}{B}}, -\frac{D}{M} \quad (6)$$

while the diagonal transfer function has two zeros:

$$z = \frac{-\frac{D}{B} \pm \sqrt{\frac{D^2}{B^2} - 4\frac{M}{B}}}{2\frac{M}{B}} \quad (7)$$

The presence of the two left-half plane (LHP) zeros in the diagonal transfer function indicates that a given generator will be more reactive to an input at that generator's bus (emulating a disturbance close to the generator in a more realistic topology) than to an input at a different generator bus (emulating a disturbance far from the generator in a more realistic topology). This is due to LHP zeros increasing a system's rise time and overshoot when subject to a step input. Therefore, the prevalence of LHP zeros in the diagonal transfer will dictate how localized the system's disturbance response is, that is, as the diagonal transfer function's zeros move further from the transfer function's poles the system will exhibit a more localized disturbance response.

The poles and zeros of the diagonal transfer function are calculated for an effective GFM inertia of 0.636 up to a value of 12.73. This covers the range of expected effective inertias of GFMs through typical values for SG inertia. A plot of how the poles and zeros of the transfer function move as inertia changes is shown in Figure 3. The real pole of the transfer function defined as $p = -\frac{D}{M}$ is omitted from this plot. As

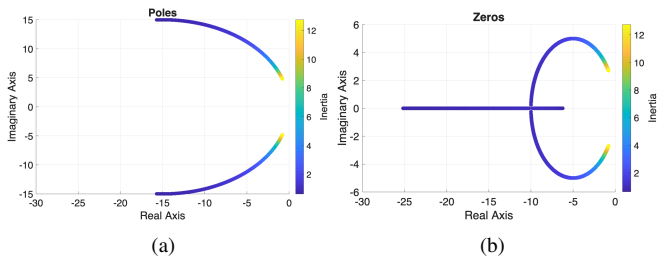


Fig. 3: (a) Complex pole location of diagonal transfer function vs. Inertia (b) Zero location of diagonal transfer function vs. inertia

inertia is increased, the complex poles of diagonal transfer function begin to approach the zeros of the transfer function. As these poles and zeros approach one another, the impact of the zeros on the transfer function's dynamics begins to diminish as does disturbance response localization behavior.

This indicates that the generator frequencies of higher inertia power systems, like those dominated by SGs, will generally move together, while low inertia power systems will see greater divergence in frequency in buses closer to the location of the disturbance.

B. H_2 -Norm Analysis

The H_2 -norm, defined as the root-mean square of a system's impulse response, for each of the derived single input-single output (SISO) transfer functions is calculated via the following definition:

$$\|H(s)\|_{H_2}^2 = \frac{1}{2\pi} \int_{-\infty}^{\infty} \|H(i\omega)\|^2 d\omega \quad (8)$$

where i represents the imaginary unit.

The following expressions for the local and nonlocal H_2 -norms are found to be:

$$\begin{aligned}\left\| \frac{\Delta\omega_i(s)}{\Delta P_{L_i}(s)} \right\|_{H_2}^2 &= \frac{6D^2 + 5BM}{12D^3M + 18BDM^2} \\ \left\| \frac{\Delta\omega_i(s)}{\Delta P_{L_j}(s)} \right\|_{H_2}^2 &= \frac{M^4}{6BD^3 + 9B^2DM}, i \neq j\end{aligned}\quad (9)$$

The derived H_2 -norm expression shows that as GFM effective inertia decreases, the local responsiveness will increase while the nonlocal responsiveness will decrease. The increase in disturbance response localization in GFM-dominated systems will influence the selection of measurement locations to be used for feedback under a WAC policy.

IV. SYSTEM CONTROLLABILITY IN ALL-GFM SYSTEMS

We now analyze how the eigenvalues of the system's controllability gramian move with respect to system parameters. Here we assume each GFM has adequate headroom for frequency response and that a WAC system is able to change the power setpoint of each GFM in the network directly. The controllability gramian is the positive definite solution to the following Lyapunov equation:

$$AW_C + W_C A^T = -BB^T \quad (10)$$

where A and B are the matrices that define the state-space implementation for the simplified network defined in Section II. The eigenvalues and eigenvectors of the controllability gramian define an ellipsoid that represents the set of states reachable with unit-energy input. The ellipsoid has semiaxis lengths equal to the square root of the eigenvalues and semiaxis directions given by the corresponding eigenvectors [8]. This implies that larger eigenvalues of the controllability gramian correspond to directions of a system that are easier to control [18]. For a system of GFMs, the controllability gramian eigenvalues and their multiplicity are given by the following theorem:

Theorem 1: Given a network of n grid-forming inverters with identical effective inertia, M , identical effective damping D , and identical line admittance coupling each inverter to every other inverter in the network, B , the eigenvalues of the controllability gramian and their multiplicity are:

- $\frac{1}{2BD}$ with multiplicity 1 associated with controlling relative GFM angles

- $\frac{1}{2nBD}$ with multiplicity $n-2$ associated with controlling relative GFM angles
- $\frac{1}{2MD}$ with multiplicity n associated with controlling GFM frequencies

The proof is given in the Appendix. This theorem implies that lower effective GFM inertia increases the controllability of GFM frequencies from the perspective of a wide-area control system. This direct connection between effective inertia and controllability will influence future work developing WAC design methods, implying that actuating GFMs will be a more effective way to control system frequencies.

V. COMPUTATIONAL ANALYSIS OF LARGER SYSTEMS

This section validates the conclusions about increased localization and controllability from Sections III and IV using larger, more realistic power system models – specifically the IEEE 39-bus and IEEE 118-bus models. The disturbance localization analysis is performed by comparing time-domain frequency response trajectories at different generators and by comparing the H_2 -norm of each load bus input to each generator frequency output. The controllability analysis is performed by numerically finding the controllability gramian eigenvalues for varying effective inertia.

A. Disturbance Localization Time Domain Analysis

A load step is applied to Bus 20 in the IEEE-39 bus system, and the resulting frequency dynamics of each of the generators is shown in Figures 4 and 5. The dynamics of the all-SG system follows the expected second-order system response of a traditional power system, with generators closer to the disturbance (generators 4 and 5) displaying greater oscillations on top of the overall system's frequency response. However, the response of the all-GFM system shows a greater heterogeneity in frequency response, with generators closer to the disturbance bus transiently diverging from the rest of the system. This indicates that all-GFM systems may experience greater localization in their load step response as compared to all-SG systems.

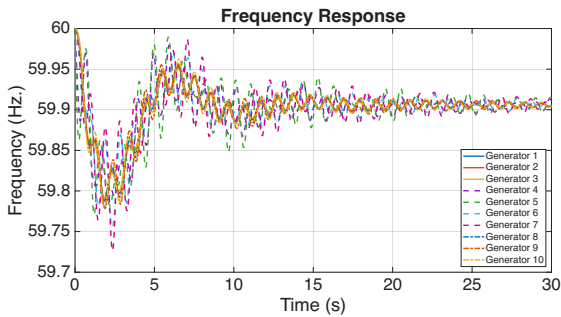


Fig. 4: IEEE 39-Bus All-SG Frequency Response for Step at Bus 20

B. Disturbance Localization H_2 -Norm Analysis

To better quantify the relationship between the disturbance location and the response of a generator, the H_2 -norm of each load bus input to each generator frequency output is

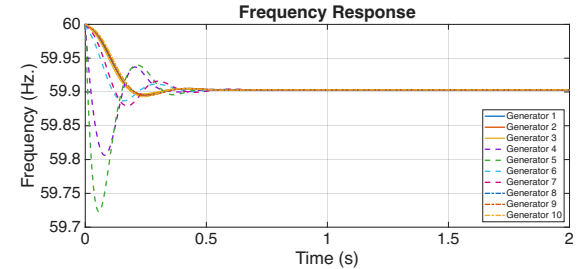


Fig. 5: IEEE 39-Bus All-GFM Frequency Response for Step at Bus 20

calculated. Each input-output H_2 -norm pair is plotted on a 2-D surface plot where each entry in the map represents how reactive a generator (the x -coordinate in the map) is to a disturbance at a load bus (the y -coordinate in the map). The calculated maps for both the all-SG and all-GFM cases of the 39-bus system are shown in Figure 6. The entries of the

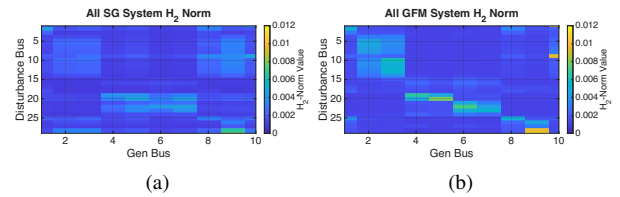


Fig. 6: IEEE 39-Bus H_2 -Norm Map of (a) All-SG System and (b) All-GFM System

H_2 -norm map of the all-GFM system corresponding to load buses and generators closer together are much greater than entries corresponding to load buses and generators further apart. This indicates that the all-GFM system will produce a more localized disturbance response. This trend is not seen in the H_2 -norm map of the all-SG system where the entries are roughly the same, meaning that each generator in the system will respond similarly to a load step regardless of location in the network. To further illustrate the effect of low inertia on localization, the time constant of the GFMs is increased by a factor of 10, creating an effective inertia closer to that of SGs. It should be noted, however, that although the effective inertia is similar to that of a SG, the GFM step response shape—dictated by the model in Figure 2—differs from that of a SG, which includes an additional feedback loop. The calculated map is provided in Figure 7. The recalculated H_2 -norm of load bus-generator relationship yields a map lacking the peaks seen in the low inertia GFM case, creating a similar structure to the all-SG case. This indicates that the localization of load step responses in all-GFM systems is driven by the speed of the GFM response caused by low effective inertia.

To verify that the localization behavior scales with larger power networks, the H_2 -norm is calculated for all-SG and all-GFM instantiations of the IEEE 118-bus system. The base 118-bus system is modified to remove any synchronous condensers. The resultant H_2 -norm maps are shown in Figure 8.

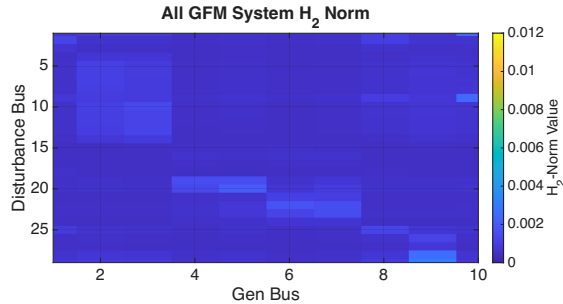


Fig. 7: IEEE 39-Bus H_2 -Norm Map of all-GFM system with slower time constant

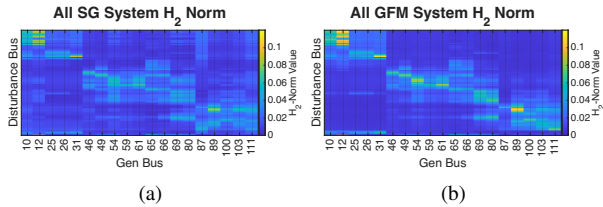


Fig. 8: IEEE 118-Bus H_2 -Norm Map of (a) All-SG System and (b) All-GFM System

Once again, the all-GFM H_2 -norm map displays higher localized peaks compared to the all-SG case, indicating that the expected localization of responses scales to larger systems. When the all-GFM 118- bus case is rerun with increased effective inertia, the peaks in the H_2 -norm map are removed, leading to a map that resembles that of the all-SG case. This further supports the idea that the lower effective inertia of GFM drives the localization of responses, even in larger power systems.

C. Controllability Analysis

To understand how the conclusions of Theorem 1 change in a more realistic network topology, the controllability gramian of the all-GFM 39-bus system model and its eigenvalues were calculated for effective inertia values from 0.636 to 12.73 under the assumption that all GFMs in the system are identical. The trend of the gramian eigenvalues as inertia is increased is shown in Figure 9. Even under more complex network topology conditions, the controllability gramian maintains the block diagonal structure used to derive the eigenvalues in the proof of Theorem 1. Therefore, the eigenvalues can be broken up into those related to controlling relative GFM phase and those related to controlling GFM frequency. Figure 9 shows eigenvalues associated with controlling frequencies are identical and scale inversely with GFM effective inertia, aligning with the conclusion drawn using a simplified network topology. Eigenvalues associated with controlling relative GFM phase angles are invariant under changes in GFM inertia, which aligns with Theorem 1. The relative angle eigenvalues, however, do not exactly match the analytical expressions given in Theorems 1 due to the more complex network topology. This result supports the main takeaway of Section IV – that the lower inertia of GFMs

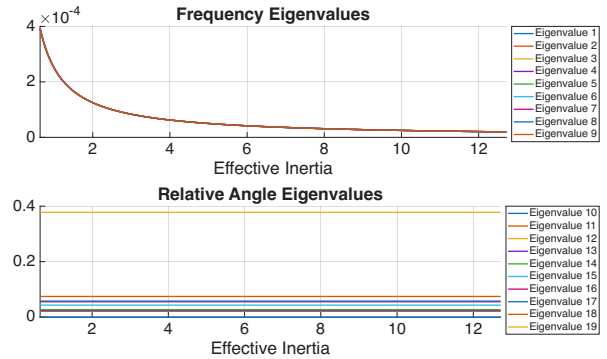


Fig. 9: Controllability Gramian Eigenvalues vs. Effective Inertia

make the frequencies of the GFMs easier to control. These findings will influence future work on WAC system design as actuation on GFMs will be more effective at controlling system frequencies due to the lower inertia properties.

VI. CONCLUSION

This paper demonstrates that the limited effective inertia of multi-loop droop GFMs leads to greater disturbance response localization in a system while also increasing the overall controllability of the inverter frequencies. The greater disturbance localization in GFM-dominated systems implies that measurements used for feedback in a WAC system will need to be close to generator nodes to capture GFM frequency response while the increase in controllability in GFM-dominated systems implies that WAC systems will be more effective when actuating GFMs. These takeaways motivate future work on developing a design method for the optimal implementation of WAC systems in modern power systems.

REFERENCES

- [1] “2024 lcoe+ report.” [Online]. Available: <https://www.lazard.com/research-insights/levelized-cost-of-energyplus/>
- [2] Y. Lin, J. H. Eto, B. B. Johnson, J. D. Flicker, R. H. Lasseter, H. N. V. Pico, G.-S. Seo, B. J. Pierre, and A. Ellis, “Research Roadmap on Grid-Forming Inverters,” p. 60. [Online]. Available: <https://www.nrel.gov/docs/fy21osti/73476.pdf>
- [3] Y. Li, Y. Gu, and T. C. Green, “Revisiting grid-forming and grid-following inverters: A duality theory,” *IEEE Transactions on Power Systems*, vol. 37, no. 6, pp. 4541–4554, 2022.
- [4] M. A. P. Peter Sauer, *Power System Dynamics and Stability*, 1st ed. USA: Stipes Publishing Co., 2007.
- [5] S. D’Arco and J. A. Sula, “Equivalence of virtual synchronous machines and frequency-droops for converter-based microgrids,” *IEEE Transactions on Smart Grid*, vol. 5, no. 1, pp. 394–395, 2014.
- [6] N. Hatzigiannou, J. Milanovic, C. Rahmann, V. Ajjarapu, C. Canizares, I. Erlich, D. Hill, I. Hiskens, I. Kamwa, B. Pal, P. Pourbeik, J. Sanchez-Gasca, A. Stankovic, T. Van Cutsem, V. Vittal, and C. Vournas, “Definition and classification of power system stability – revisited and extended,” *IEEE Transactions on Power Systems*, vol. 36, no. 4, pp. 3271–3281, 2021.
- [7] A. Chakrabortty and P. P. Khargonekar, “Introduction to wide-area control of power systems,” in *2013 American Control Conference*, 2013, pp. 6758–6770.
- [8] G. Lindmark and C. Altafini, “Minimum energy control for complex networks,” *Scientific Reports*, vol. 8, no. 1, p. 3188, Feb 2018. [Online]. Available: <https://doi.org/10.1038/s41598-018-21398-7>

- [9] F. Pasqualetti, S. Zampieri, and F. Bullo, "Controllability metrics, limitations and algorithms for complex networks," *IEEE Transactions on Control of Network Systems*, vol. 1, no. 1, pp. 40–52, 2014.
- [10] Y.-S. Li, D.-Z. Ma, H.-G. Zhang, and Q.-Y. Sun, "Critical nodes identification of power systems based on controllability of complex networks," *Applied Sciences*, vol. 5, no. 3, pp. 622–636, 2015.
- [11] J. Li, L. Dueñas-Osorio, C. Chen, B. Berryhill, and A. Yazdani, "Characterizing the topological and controllability features of U.S. power transmission networks," *Physica A: Statistical Mechanics and its Applications*, vol. 453, pp. 84–98, 2016.
- [12] S. Roy, S. G. Aksoy, S. Sarker, P. Wang, and S. J. Young, "Structural controllability assessment for inverter-based microgrids," in *2021 North American Power Symposium (NAPS)*, 2021, pp. 1–6.
- [13] Y. Zhan, X. Xie, and Y. Wang, "Impedance network model based modal observability and controllability analysis for renewable integrated power systems," *IEEE Transactions on Power Delivery*, vol. 36, no. 4, pp. 2025–2034, 2021.
- [14] F. Paganini and E. Mallada, "Global analysis of synchronization performance for power systems: Bridging the theory-practice gap," *IEEE Transactions on Automatic Control*, vol. 65, no. 7, pp. 3007–3022, 2020.
- [15] M. Trujillo, A. Sajadi, J. Shaw, and B.-M. Hodge, "Computationally efficient analytical models of frequency and voltage in low-inertia systems," 2025. [Online]. Available: <https://arxiv.org/abs/2506.06620>
- [16] L. Qiu, M. Gu, Z. Chen, Z. Du, L. Zhang, W. Li, J. Huang, and J. Fang, "Oscillation suppression of grid-following converters by grid-forming converters with adaptive droop control," *Energy*, vol. 17, no. 20, 2024.
- [17] E. Tegling, B. Bamieh, and D. F. Gayme, "The price of synchrony: Evaluating the resistive losses in synchronizing power networks," *IEEE Transactions on Control of Network Systems*, vol. 2, no. 3, 2015.
- [18] R. Kalman, Y. C. Ho, and K. S. Narendra, "Controllability of linear dynamical systems," *Contrib. Differential Equations*, vol. 1, pp. 189–213, 1962.

APPENDIX

To derive the expressions for the controllability eigenvalues, the controllability gramian must be determined. The Lyapunov equation of the controllability gramian is:

$$\begin{bmatrix} A_{11} & A_{12} \\ A_{21} & A_{22} \end{bmatrix} \begin{bmatrix} W_{11} & W_{12} \\ W_{21} & W_{22} \end{bmatrix} + \begin{bmatrix} W_{11} & W_{12} \\ W_{21} & W_{22} \end{bmatrix} \begin{bmatrix} A_{11}^T & A_{12}^T \\ A_{21}^T & A_{22}^T \end{bmatrix} = \begin{bmatrix} B_{11} & B_{12} \\ B_{21} & B_{22} \end{bmatrix} \quad (11)$$

The expressions of each nonzero block matrix in the above expression are as follows:

$$A_{21}(i, j) = \begin{cases} \frac{A_{12}}{M} & \text{for } i = j \text{ and } i, j \in \{1, \dots, n-1\} \\ \frac{-(n-1)B}{M} & \text{else} \end{cases} \quad (12)$$

$$A_{22} = \frac{-D}{M} I_n, \quad B_{22} = \frac{-1}{M^2} I_n$$

A_{11}, B_{11}, B_{12} , and B_{21} will be matrices of all 0, (11) may be rewritten as the following system of equations:

$$\begin{aligned} A_{12}W_{21} + W_{12}A_{21}^T &= 0, & A_{21}W_{11} + W_{22}A_{12}^T &= 0 \\ A_{12}W_{22} + W_{11}A_{21}^T &= 0, & A_{22}W_{22} + W_{22}A_{22}^T &= B_{22} \end{aligned} \quad (13)$$

Since the controllability gramian, W_C , will be a unique solution, we assume W_{12} and W_{21} are zero matrices to satisfy the first expression. If expressions for W_{11} and W_{22} are obtainable under this assumption then the assumption is proven correct. Under identical coupling and GFM parameter assumptions in a simplified network, B_{22} becomes $B_{22} = \frac{-1}{M^2} I_n$. Since A_{22} is diagonal, the last expression in (13) can be written as:

$$2A_{22}W_{22} = \frac{-1}{M^2} I_n \quad (14)$$

Substituting the expression for A_{22} , the expression becomes:

$$2 \frac{-D}{M} W_{22} = \frac{-1}{M^2} I_n \quad (15)$$

Therefore, W_{22} is found to be $W_{22} = \frac{1}{2MD} I_n$.

Substituting the third expression with the known expressions for A_{12}, A_{21} , and W_{22} yields:

$$\begin{aligned} & \frac{1}{2MD} [I_{n-1} \ -1_{n-1 \times 1}] \\ &= -W_{11} \frac{B}{M} [1_{n-1 \times n-1} \ -nI_{n-1} \ 1_{n-1 \times 1}] \end{aligned} \quad (16)$$

When expanding the above expression column-wise, the final column implies the following property of the columns of W_{11} :

$$\sum_{i=1}^n w_{11,i} = \frac{1}{2BD} \cdot 1_{n-1 \times 1} \quad (17)$$

That is, the columns of W_{11} must sum to a column vector in which all entries are equal to $\frac{1}{2BD}$.

The expression for the columns can also be written as:

$$\frac{1}{2BD} e_j = (n-1)w_{11,j} - \sum_{i \neq j}^{n-1} w_{11,i} \text{ for } j \in \{1, \dots, n\}, \quad (18)$$

where e_j is the j -th unit vector of the canonical basis. The condition on the summation of the columns of W_{11} is used to substitute the summation term, yielding:

$$\begin{aligned} & \frac{1}{2BD} e_j = (n-1)w_{11,j} \\ & - \left(\frac{1}{2BD} \cdot 1_{n-1 \times 1} - w_{11,j} \right) \text{ for } j \in \{1, \dots, n\} \end{aligned} \quad (19)$$

The expression for the j -th column of W_{11} is then:

$$w_j = \frac{1}{2BD} (e_j + 1_{n-1 \times 1}) \quad (20)$$

The complete expression for the controllability gramian, W_C , is:

$$W_C = \begin{bmatrix} \frac{1}{2nBD} (1_{n-1 \times n-1} + I_{n-1}) & 0_{n-1 \times n} \\ 0_{n \times n-1} & \frac{1}{2MD} I_n \end{bmatrix} \quad (21)$$

Since W_C is block diagonal, its eigenvalues are simply those of its two diagonal blocks: the upper-left block, associated with the first $n-1$ states (GFM relative phase angles), and the lower-right block, associated with the remaining n states (GFM frequencies). The upper-left block has one eigenvalue equal to $\frac{1}{2BD}$ and $n-2$ eigenvalues equal to $\frac{1}{2nBD}$. The lower-right block is diagonal, so its eigenvalues are its diagonal entries, yielding n eigenvalues of $\frac{1}{2MD}$.